



## Fe<sub>2</sub>O<sub>3</sub>-TiO<sub>2</sub> Nano-heterostructure Photoanodes for Highly Efficient Solar Water Oxidation

### Citation

Barreca, D., Carraro, G., Gasparotto, A., Maccato, C., Warwick, M. E. A., Kaunisto, K., ... Mathur, S. (2015). Fe<sub>2</sub>O<sub>3</sub>-TiO<sub>2</sub> Nano-heterostructure Photoanodes for Highly Efficient Solar Water Oxidation. *Advanced Materials Interfaces*, 2(17). <https://doi.org/10.1002/admi.201500313>

### Year

2015

### Version

Peer reviewed version (post-print)

### Link to publication

[TUTCRIS Portal \(http://www.tut.fi/tutcris\)](http://www.tut.fi/tutcris)

### Published in

Advanced Materials Interfaces

### DOI

[10.1002/admi.201500313](https://doi.org/10.1002/admi.201500313)

### Copyright

This is the peer reviewed version of the following article: Barreca D., Carraro G., Gasparotto A., Maccato C., Warwick M. E. A., Kaunisto K., Sada C., Turner S., Gönüllü Y., Ruoko Tero-Petri, Borgese L., Bontempi E., Tendeloo G. V., Lemmetyinen H., Mathur S. (2015). Fe<sub>2</sub>O<sub>3</sub>-TiO<sub>2</sub> Nano-heterostructure Photoanodes for Highly Efficient Solar Water Oxidation. *Adv. Mater. Interfaces*, 2: 1500313, which has been published in final form at <https://dx.doi.org/10.1002/admi.201500313>. This article may be used for non-commercial purposes in accordance with Wiley Terms and Conditions for Self-Archiving.

### Take down policy

If you believe that this document breaches copyright, please contact [cris.tau@tuni.fi](mailto:cris.tau@tuni.fi), and we will remove access to the work immediately and investigate your claim.

DOI: 10.1002/ ((please add manuscript number))

**Article type:** Full paper

**Fe<sub>2</sub>O<sub>3</sub>-TiO<sub>2</sub> nano-heterostructure photoanodes for highly efficient solar water oxidation**

By *Davide Barreca*,\* *Giorgio Carraro*, *Alberto Gasparotto*, *Chiara Maccato*, *Michael E.A. Warwick*, *Kimmo Kaunisto*,\* *Cinzia Sada*, *Stuart Turner*, *Yakup Gönüllü*, *Tero-Petri Ruoko*, *Laura Borgese*, *Elza Bontempi*, *Gustaaf Van Tendeloo*, *Helge Lemmetyinen*, and *Sanjay Mathur*

[\*] Dr. D. Barreca

CNR-IENI and INSTM, Department of Chemistry, Padova University, 35131 Padova, Italy.

E-mail: [davide.barreca@unipd.it](mailto:davide.barreca@unipd.it)

Dr. G. Carraro, Dr. A. Gasparotto, Prof. C. Maccato, Dr. M.E.A. Warwick

Department of Chemistry, Padova University and INSTM, 35131 Padova, Italy.

[\*] Dr. K. Kaunisto, Mr. T.-P. Ruoko, Prof. H. Lemmetyinen

Department of Chemistry and Bioengineering, Tampere University of Technology, 33101 Tampere, Finland.

E-mail: [kimmo.kaunisto@tut.fi](mailto:kimmo.kaunisto@tut.fi)

Prof. C. Sada

Department of Physics and Astronomy, Padova University, 35131 Padova, Italy.

Dr. S. Turner, Prof. G. Van Tendeloo

EMAT, University of Antwerp, 2020 Antwerpen, Belgium.

Dr. Y. Gönüllü, Prof. S. Mathur

Department of Chemistry, Chair of Inorganic and Materials Chemistry, Cologne University, 50939 Cologne, Germany.

Dr. L. Borgese, Prof. E. Bontempi

Chemistry for Technologies Laboratory, University of Brescia, 25123 Brescia, Italy.

**Keywords:** Fe<sub>2</sub>O<sub>3</sub>; TiO<sub>2</sub>; nano-heterostructures; water splitting; photoelectrochemistry.

**Abstract:** Harnessing solar energy for the production of clean hydrogen by photoelectrochemical (PEC) water splitting represents a very attractive, but challenging approach for sustainable energy generation. In this regard, we report on the fabrication of Fe<sub>2</sub>O<sub>3</sub>-TiO<sub>2</sub> photoanodes, showing attractive performances [ $\approx 2.0 \text{ mA cm}^{-2}$  at 1.23 V vs. the reversible hydrogen electrode (RHE) in 1 M NaOH] under simulated one-sun illumination. This goal, corresponding to a 10-fold photoactivity enhancement with respect to bare Fe<sub>2</sub>O<sub>3</sub>, is achieved by atomic layer deposition (ALD) of TiO<sub>2</sub> over *hematite* ( $\alpha$ -Fe<sub>2</sub>O<sub>3</sub>) nanostructures fabricated by plasma enhanced-chemical vapor deposition (PE-CVD), and final annealing at 650°C. The adopted approach enables an intimate Fe<sub>2</sub>O<sub>3</sub>-TiO<sub>2</sub> coupling, resulting in an electronic interplay at the Fe<sub>2</sub>O<sub>3</sub>/TiO<sub>2</sub> interface. The reasons for the photocurrent enhancement determined by TiO<sub>2</sub> overlayers with increasing thickness are unraveled by a detailed chemico-physical investigation, as well as by the study of photogenerated charge carrier dynamics. Transient absorption spectroscopy shows that **the increased PEC responses of heterostructured photoanodes compared to bare hematite are mainly due to an enhanced separation of photogenerated charge carriers**. The obtainment of stable responses even in simulated seawater provides a feasible route in view of the eventual large-scale generation of renewable energy.

## 1. Introduction

The development of sustainable energy production systems has become an ever-growing demand under the rising stress of the global population, living standards and increased industrialization.<sup>[1-7]</sup> In this context, photo-activated methods such as photoelectrochemical (PEC) H<sub>2</sub>O splitting, starting from two abundant natural resources such as solar photons and water, are environmentally benign approaches for the production of hydrogen as a clean and renewable energy vector.<sup>[8-24]</sup> A key issue for PEC water splitting is the identification of suitable photoanode materials satisfying the challenging requirements for solar hydrogen generation.<sup>[13,14,25,26]</sup> Among the most promising candidates, *hematite* ( $\alpha$ -Fe<sub>2</sub>O<sub>3</sub>) has long been a preferred choice<sup>[18,20,27-32]</sup> thanks to its good photochemical stability, earth abundance, non-toxicity, low cost and proper band gap ( $E_G \approx 2.1$  eV) to absorb a large fraction of the solar spectrum.<sup>[3,4,16,21,33-36]</sup> In spite of these advantages, the solar-to-hydrogen efficiency of *hematite* falls well short of the theoretical maximum value ( $\approx 13\%$ )<sup>[6,7,10,11,34,37]</sup> due to a number of factors,<sup>[2,12,17,25,30,38]</sup> including poor transport properties, improper band positions for unassisted water splitting, low electron-hole pair lifetime ( $< 10$  ps) and small exciton diffusion length ( $\approx 2$ -4 nm).<sup>[11,28,35,39,40]</sup> To overcome these drawbacks and enhance *hematite* conductivity and photoresponses, the most commonly used strategies are nanoarchitecture engineering<sup>[7,11,18,22,26,39]</sup> and elemental doping.<sup>[17,25,29,41,42]</sup> Other improvements have been afforded by the introduction of oxygen evolution catalysts (OECs), such as Co-, Ni-, Ir- and Ru-based ones.<sup>[1,10,19,24-26,43]</sup> Despite the advantageous reduction in the onset potential, most of these systems are toxic and/or expensive, being unsuitable for large-scale energy production. In addition, water oxidation efficiencies are often limited by surface recombination, a severe issue to be tackled.<sup>[19,26,44]</sup> An alternative strategy to address the primary requirements for an efficient solar-to-hydrogen conversion consists in the formation of nano-heterostructures involving Fe<sub>2</sub>O<sub>3</sub> coupling with suitable under- or overlayers,<sup>[1,4,33,40,45,46]</sup> to suppress electron back-recombination at the *hematite*/substrate interface,<sup>[20,28,29]</sup> enhance light absorption and improve carrier transport

properties.<sup>[5,16,19,27,47]</sup> So far, several works have been focused on the surface functionalization of Fe<sub>2</sub>O<sub>3</sub> nanosystems with various oxides, such as Al<sub>2</sub>O<sub>3</sub>, Ga<sub>2</sub>O<sub>3</sub>, Fe<sub>x</sub>Sn<sub>1-x</sub>O<sub>4</sub>, and TiO<sub>2</sub>.<sup>[3,10,19,20,39]</sup> The obtained results highlight the possibility of improving PEC performances by passivation of surface states, protection against corrosion, use of buried semiconductor junctions,<sup>[2,19]</sup> and a proper tailoring of charge transfer processes between the constituent phases.<sup>[20,47]</sup> Nevertheless, the practical use of modified *hematite* photoanodes in efficient, durable, and low-cost solar hydrogen production is still hindered by various factors,<sup>[37]</sup> including the system stability<sup>[29]</sup> and the difficulties in identifying precise structure-functions relationships.<sup>[6,17]</sup> In addition, driving PEC water splitting more efficiently than the state-of-the-art *hematite* photoanodes<sup>[48]</sup> remains a main hurdle impeding further technological developments.<sup>[34]</sup>

In the present study, we report on a method for the enhancement of *hematite* photoanode charge transfer, resulting in a remarkable improvement of the recorded PEC performances in solar water splitting. In particular, we have devoted our attention to the coating of PE-CVD *hematite* nanostructures by an ALD TiO<sub>2</sub> overlayer, followed by thermal treatment in air at 650°C. It is worth highlighting that, despite several efforts aimed at investigating Ti incorporation into *hematite* photoelectrodes,<sup>[7,29,35,38,40,42]</sup> Fe<sub>2</sub>O<sub>3</sub>-TiO<sub>2</sub> multi-layered and composite systems have so far been much less investigated.<sup>[3,6,16,27,45]</sup> For these materials, the current density for water photooxidation has been reported to drop off with an increased number of TiO<sub>2</sub> ALD cycles, the reasons underlying this behavior being unclear.<sup>[2]</sup> In this work, taking advantage of ALD repeatability, conformality and precise thickness control,<sup>[24,46,49]</sup> we focus our attention on the PEC behavior of Fe<sub>2</sub>O<sub>3</sub>-TiO<sub>2</sub> nano-heterostructures characterized by different TiO<sub>2</sub> overlayer thicknesses. A relevant attention is devoted to the interrelations between system properties and functional performances, with particular regard to the structural and electronic interplay occurring at Fe<sub>2</sub>O<sub>3</sub>/TiO<sub>2</sub> heterointerfaces. Under optimized conditions, a 10-fold photocurrent increase compared to bare  $\alpha$ -Fe<sub>2</sub>O<sub>3</sub> photoanodes was observed, corresponding to the highest performances ever reported for similar systems, especially at high applied potentials. This feature, along with the high stability even in simulated seawater, for

which solar splitting has only been seldom investigated,<sup>[50]</sup> represents an important goal towards the sustainable and efficient conversion of solar light into chemical energy.

## 2. Results and Discussion

### 2.1 Preparation and Characterization of Fe<sub>2</sub>O<sub>3</sub>-TiO<sub>2</sub> photoanodes

Fe<sub>2</sub>O<sub>3</sub>-TiO<sub>2</sub> photoanodes were fabricated by a three-step protocol, involving: i) PE-CVD of Fe<sub>2</sub>O<sub>3</sub> on fluorine-doped tin oxide (FTO) substrates; ii) ALD of TiO<sub>2</sub> with a different cycle numbers, in order to tailor the corresponding overlayer thickness, and iii) annealing in air for 1 h at 650°C (Table 1). Bare Fe<sub>2</sub>O<sub>3</sub> (hereafter labeled as Fe<sub>2</sub>O<sub>3</sub>), composed of pure  $\alpha$ -Fe<sub>2</sub>O<sub>3</sub> (*hematite*) free from other iron oxide polymorphs, was characterized by an inherently porous nano-organization [Supporting Information (SI), Figure S1]. The subsequent ALD of TiO<sub>2</sub> resulted in morphological variations, as revealed by field emission-scanning electron microscopy (FE-SEM; see Figure 1). In particular, specimens 400\_L and 400\_H, obtained with a lower and a higher number of ALD cycles, presented more rounded surface features than the pristine Fe<sub>2</sub>O<sub>3</sub> (SI, Figures S1a-b). In the case of 400\_L, functionalization with TiO<sub>2</sub> produced only a modest alteration of Fe<sub>2</sub>O<sub>3</sub> aggregate features, indicating the formation of a conformal thin film. For specimen 400\_H, more marked modifications of the surface morphology took place (Figures 1a-b). The system double-layered structure was clearly evidenced by cross-sectional FE-SEM images (Figures 1c-d). As can be observed, upon going from specimen 400\_L to the homologous 400\_H, the TiO<sub>2</sub> overlayer thickness underwent a parallel increase. These observations, along with the intimate and uniform Fe<sub>2</sub>O<sub>3</sub>-TiO<sub>2</sub> contact, highlight the intrinsic ALD conformal coverage capability,<sup>[18,19,49]</sup> enabling a fine control of the resulting Fe<sub>2</sub>O<sub>3</sub>-TiO<sub>2</sub> heterojunction features. Cross sectional FE-SEM images enabled the estimation of the total nanodeposit (and *titania* overlayer) thickness values, yielding  $400 \pm 15$  ( $35 \pm 10$ ) and  $480 \pm 30$  ( $80 \pm 10$ ) nm for 400\_L and 400\_H, respectively. In order to attain a further insight into the system topography, the material surfaces were probed by atomic force microscopy (AFM; Figures 1g-h). The recorded micrographs showed the formation of multi-grain structures, in line with FE-SEM

observations. Irrespective of the synthesis conditions, very similar root-mean-square (RMS) roughness values ( $\approx 20$  nm) were obtained for the analyzed systems.

The local in-depth composition was analysed by energy dispersive X-ray spectroscopy (EDXS) line-scans (Figures 1e-f). The obtained data showed that  $\text{TiO}_2$  was mainly concentrated in the outermost material region, a phenomenon more evident for the 400\_H sample, confirming that a higher number of ALD cycles resulted in a thicker  $\text{TiO}_2$  overlayer, as already appreciated by FE-SEM images. Conversely, the  $\text{FeK}\alpha$  line intensity underwent a progressive increase in the inner system region at the expense of the  $\text{TiK}\alpha$  one, confirming the predominance of  $\text{Fe}_2\text{O}_3$  in the deposit regions closer to the FTO substrate.

Since the mutual spatial distribution of  $\text{Fe}_2\text{O}_3$  and  $\text{TiO}_2$  is a key issue for an optimal heterostructure engineering, the in-depth chemical composition along the thickness was further investigated by secondary ion mass spectrometry (SIMS) analyses (Figures 2a-b). The obtained data allowed the estimation of a mean C concentration (averaged over the whole thickness) as low as 150 ppm, highlighting thus the purity of the obtained materials. Irrespective of the processing conditions, the O ionic yield remained almost constant throughout the investigated depth. As can be observed in Figure 2, the outermost sample region was Ti-rich, a phenomenon particularly evident for specimen 400\_H, characterized by a higher thickness of the  $\text{TiO}_2$  overlayer. Upon increasing the sputtering time, a concomitant increase in the Fe ionic yield and a progressive decrease in the Ti one took place, in agreement with EDXS data (see Figure 1). This evidence suggested that the  $\text{TiO}_2$  layer was covering *hematite* nanostructures even in the inner regions, a phenomenon due to the synergy between the  $\text{Fe}_2\text{O}_3$  porosity and the good conformality achievable by the use of ALD. Finally, both titanium and iron signals underwent a net intensity decrease at the interface with the FTO substrate. The Sn tailing extending into the nanodeposits at the interfacial region suggested the occurrence of tin diffusion from the FTO substrate induced by thermal annealing, at least to some extent. This phenomenon, already observed in previous works, might beneficially contribute to PEC performances, due to an improved

system electrical conductivity.<sup>[37,43,51]</sup>

Overall, the data discussed so far point to the obtainment of Fe<sub>2</sub>O<sub>3</sub>-TiO<sub>2</sub> heterostructures, with titanium oxide being mainly confined in the outermost system regions. To perform a detailed characterization of the Fe and Ti chemical environments, X-ray photoelectron spectroscopy (XPS) analyses were carried out. Wide-scan XPS spectra (SI, Figure S2a) were dominated by titanium and oxygen photopeaks. In the case of sample 400\_L, the presence of iron could also be detected (see Figure 2d), suggesting in this case the occurrence of a thinner and porous TiO<sub>2</sub> overlayer (compare TEM analysis; see below). Irrespective of the used ALD conditions, the Ti2p<sub>3/2</sub> binding energy (BE) of 458.5 eV, as well as the separation between the spin-orbit components [ $\Delta(\text{BE}) = 5.7$  eV] (Figure 2c), were in line with the presence of Ti(IV) in TiO<sub>2</sub>.<sup>[35,52]</sup> The Fe2p peak shape and position [Figure 2d; BE(Fe2p<sub>3/2</sub>) = 711.1 eV], along with the pertaining spin-orbit splitting [ $\Delta(\text{BE}) = 13.7$  eV], were consistent with the formation of iron(III) oxide free from other Fe oxidation states.<sup>[7,11,33,35,42,52]</sup> The O1s signal (SI, Figure S2b) could be fitted by two contributing bands located at BE = 530.0 eV (I) and 532.0 eV (II), attributed to lattice O and surface -OH groups/adsorbed oxygen.<sup>[4,7,35,42]</sup>

The structure of the deposited Fe<sub>2</sub>O<sub>3</sub>-TiO<sub>2</sub> photoanodes was investigated by X-ray diffraction (XRD). The recorded patterns (SI, Figure S3) were dominated by a series of signals corresponding to *hematite* reflections for both specimens 400\_L and 400\_H.<sup>[53]</sup> Interestingly, the latter also showed the appearance of additional peaks at  $2\theta = 25.3$  and  $47.9^\circ$ , related to (101) and (200) crystallographic planes of *anatase* TiO<sub>2</sub>,<sup>[54]</sup> whereas no signals related to *titania* could be unambiguously observed for sample 400\_L, due to the lower amount of deposited TiO<sub>2</sub> (compare the thickness values obtained by cross-sectional FE-SEM analyses, see above). In accordance with XPS results, no reflections related to Fe-Ti-O ternary phases were present, and the absence of appreciable angular shifts also enabled to rule out the occurrence of Ti doping into Fe<sub>2</sub>O<sub>3</sub>.

To investigate the nanoscale structure of Fe<sub>2</sub>O<sub>3</sub>-TiO<sub>2</sub> materials, (high resolution)-transmission

electron microscopy (HR)-TEM, high angle annular dark field-scanning transmission electron microscopy (HAADF-STEM) and EDXS analyses were carried out. Figures 3a-d display HAADF-STEM (Z-contrast) overview images of both samples in cross-section, together with EDXS elemental maps for Ti, Fe, Sn and Si, evidencing the glass/FTO/ $\alpha$ -Fe<sub>2</sub>O<sub>3</sub>/TiO<sub>2</sub> multi-layer stacks. The Fe<sub>2</sub>O<sub>3</sub>/TiO<sub>2</sub> interface is imaged in more detail in Figures 3e-f, from which TiO<sub>2</sub> overlayer thickness values were extracted and were in excellent agreement with those provided by FE-SEM analyses (see above and Figure 1). Irrespective of the used ALD conditions, the Fe<sub>2</sub>O<sub>3</sub> nanodeposit consisted of well-developed upward growing *hematite* needles, whose assembly resulted in an open, porous structure. This peculiar texture enabled the ALD TiO<sub>2</sub> coating to be deposited even in the inner system regions, confirming the formation of Fe<sub>2</sub>O<sub>3</sub>-TiO<sub>2</sub> nano-heterostructures. The overlayers, composed by TiO<sub>2</sub> with the *anatase* crystal phase, are further imaged by the HR micrographs reported in Figures 3g-h. The presence of small voids (mean size of few nanometers), imaged as a dark contrast in the mass-thickness sensitive HAADF-STEM view in Figure 3h, highlights the porosity of the *titania* top layer. Electron diffraction (ED) maps of both specimens showed reflections that could be attributed to *hematite* and *anatase* phases (see SI, Figures S4), despite the 400\_L sample displayed very weak *anatase* signals due to the low TiO<sub>2</sub> amount (see also XRD data).

The target Fe<sub>2</sub>O<sub>3</sub>/TiO<sub>2</sub> nano-heterostructures were also analyzed by optical absorption spectroscopy (SI, Figure S5). The recorded spectra were characterized by a sub-band-gap scattering tail in the 600–750 nm region, and a sharp absorbance increase occurring from 550–600 nm towards lower wavelengths, consistent with the band-gap of *hematite*.<sup>[25,40,43]</sup> As a whole, the optical properties of the present Fe<sub>2</sub>O<sub>3</sub>-TiO<sub>2</sub> heterostructures are appealing for PEC water splitting triggered by solar irradiation, since these photoanodes can efficiently absorb a significant fraction of the Vis spectrum. From Tauc plots, it was possible to extrapolate a mean band gap ( $E_G$ ) value of 2.1 eV, revealing that the TiO<sub>2</sub> overlayers did not appreciably affect the optical features in the Vis range.<sup>[16,17,38,44]</sup>

## 2.2 PEC investigation of Fe<sub>2</sub>O<sub>3</sub>-TiO<sub>2</sub> photoanodes

The functional properties of Fe<sub>2</sub>O<sub>3</sub>-TiO<sub>2</sub> heterostructures in PEC water splitting were evaluated in NaOH aqueous solutions (Figure 4a) and compared with those of a bare Fe<sub>2</sub>O<sub>3</sub> photoelectrode. In the absence of illumination, the samples showed very small photocurrents, and even when the current onset potential ( $E_{\text{onset}}$ ) for water oxidation reaction was reached at  $\approx 1.8$  V,<sup>[5]</sup> dark currents were lower than 1 mA cm<sup>-2</sup>. Upon simulated solar illumination, a net  $j$  increase at potentials lower than  $E^\circ$  (1.23 V vs. RHE) took place, since part of the energy required for the oxidation process is captured from the incident light.<sup>[5]</sup> Considering  $E_{\text{onset}}$  as the value at which a current density of 0.02 mA cm<sup>-2</sup> is first reached,<sup>[6]</sup> for the pure Fe<sub>2</sub>O<sub>3</sub> photoanode  $E_{\text{onset}}$  was estimated to be 1.1 V<sub>RHE</sub>. Subsequently, a progressive  $j$  increase with  $E$  occurred, reaching a value of 0.24 mA cm<sup>-2</sup> at 1.23 V<sub>RHE</sub>. As can be observed, the functionalization of *hematite* with TiO<sub>2</sub> resulted in a decrease of the onset potential and in a significant increase of the recorded photocurrent values. Interestingly, a dependence of PEC performances on TiO<sub>2</sub> thickness could be clearly appreciated, since sample 400\_H displayed a systematic enhancement of photocurrent values with respect to the 400\_L one. In particular, 400\_H showed an  $E_{\text{onset}}$  value as low as 0.8 V<sub>RHE</sub> and  $j = 2.0$  mA cm<sup>-2</sup> at 1.23 V<sub>RHE</sub>, a value nearly ten times higher than that pertaining to pure Fe<sub>2</sub>O<sub>3</sub>. It is generally accepted that the required overpotential is related to the poor oxygen evolution reaction (OER) kinetics and to the unfavorable conduction band energy position for bare Fe<sub>2</sub>O<sub>3</sub>.<sup>[5,6,19,46]</sup> As a consequence, the shift of  $E_{\text{onset}}$  to more cathodic potentials highlights the beneficial effect exerted by TiO<sub>2</sub> functionalization on the system photoresponse. Along with the onset potential, one of the most important parameters to evaluate photoanode performances is represented by the photocurrent value plateau. In this regard, bare Fe<sub>2</sub>O<sub>3</sub> reached a plateau at  $\approx 1.4$  V ( $j \approx 0.6$  mA cm<sup>-2</sup>), whereas Fe<sub>2</sub>O<sub>3</sub>-TiO<sub>2</sub> systems did not display any appreciable saturation up to 1.8 V vs. RHE ( $j \approx 9.6$  mA cm<sup>-2</sup> for specimen 400\_H). Basing on the above observations, the higher photocurrents for samples 400\_L and 400\_H, as well as the absence of saturation effects at potentials higher than 1.23 V vs. RHE, can be traced back to the **formation of Fe<sub>2</sub>O<sub>3</sub>-TiO<sub>2</sub> heterojunctions, responsible for a more efficient charge carrier**

**separation with respect to bare Fe<sub>2</sub>O<sub>3</sub>.**<sup>[5]</sup> In particular, at 1.23 V<sub>RHE</sub>, a *j* value close to 2.0 mA cm<sup>-2</sup> was recorded for the 400\_H specimen. This photocurrent threshold compares very favorably with the best values reported in the literature for Fe<sub>2</sub>O<sub>3</sub>-TiO<sub>2</sub> photoelectrodes.<sup>[4,6,14,15,19,32,50]</sup> Such a result, obtained without the use of any expensive/toxic co-catalyst, is very attractive in view of solar water splitting promoted by Fe<sub>2</sub>O<sub>3</sub>-TiO<sub>2</sub> materials.

In order to elucidate the role of the TiO<sub>2</sub> overlayer, solar-to-hydrogen (STH) efficiency values were calculated from *j*-*E* data. It is worth noting that only a few works in the available literature report STH values for similar systems.<sup>[34]</sup> As can be appreciated from Figure 4b, the STH efficiency maximum increased in the order: **Fe<sub>2</sub>O<sub>3</sub>** (0.007 %) < **400\_L** (0.060 %) < **400\_H** (0.098 %). Notably, the highest photoefficiency values were obtained for TiO<sub>2</sub>-containing specimens at *E* values lower than for bare Fe<sub>2</sub>O<sub>3</sub>. **This finding highlights the beneficial effect of the Fe<sub>2</sub>O<sub>3</sub>-TiO<sub>2</sub> heterojunction in determining an improved charge separation of photogenerated charge carriers (see also below). To further support this observation, it is worthwhile noticing that the PEC response (SI, Figure S6) of bare TiO<sub>2</sub>, fabricated by ALD and annealed at 650°C, upon solar irradiation is almost negligible, indicating that the TiO<sub>2</sub> layer as such is indeed not photoactive.**

It is well known that the main drawbacks related to the use of Fe<sub>2</sub>O<sub>3</sub> photoanodes include the high density of surface states, low hole mobility, short charge carrier lifetime and slow OER kinetics.<sup>[2,50]</sup> On the other hand, even TiO<sub>2</sub> photoanodes suffer from various disadvantages, in particular, from a poor solar light harvesting.<sup>[3,45]</sup> So far, some studies have demonstrated that functionalization of Fe<sub>2</sub>O<sub>3</sub> with TiO<sub>2</sub> results in worse PEC performances with respect to bare iron(III) oxide.<sup>[2,19,50]</sup> In a different way, the very high photocurrents shown by the present Fe<sub>2</sub>O<sub>3</sub>/TiO<sub>2</sub> photoanodes, along with the decreased onset voltages and the absence of significant saturation at high applied potentials, highlight the benefit offered by Fe<sub>2</sub>O<sub>3</sub>/TiO<sub>2</sub> heterojunctions in affording favorable photoactivity improvements.<sup>[3,16,27,47]</sup> Due to the mutual positions of Fe<sub>2</sub>O<sub>3</sub> and TiO<sub>2</sub> conduction band edges, electrons photogenerated in TiO<sub>2</sub> can be easily transferred to Fe<sub>2</sub>O<sub>3</sub> **and injected into**

**the FTO substrate, and can subsequently migrate** through the external electric circuit to reduce water at the cathode,<sup>[45]</sup> suppressing thus detrimental recombination effects (see also below and Scheme 1). **An additional favorable contribution** to the actual performances is related to the fact that TiO<sub>2</sub> overlayers can prevent *hematite* photocorrosion in a wide pH range.<sup>[5]</sup>

To attain an insight into the stability of the present materials, PEC measurements were carried out under the same conditions at the 1<sup>st</sup> and 3<sup>rd</sup> day of utilization for the best performing system, *i.e.*, specimen 400\_H. The obtained experimental results (SI, Figure S7) revealed that the measured photocurrent values did not undergo any appreciable variation, evidencing a good stability of the target photoanodes, a key prerequisite for their technological applications.

Basing on these very favorable results, the most efficient and promising photoelectrode (**400\_H**) was tested in PEC water splitting using simulated seawater solutions. The use of seawater represents a key technological target for a real-world sustainable hydrogen generation, since 97.5% of the overall H<sub>2</sub>O available on earth is salt water.<sup>[55,56]</sup> Figure 4c compares *j-E* curves obtained using simulated seawater upon solar illumination for specimen 400\_H and for bare Fe<sub>2</sub>O<sub>3</sub>. As can be observed, for the latter, an increase in photocurrent densities with the applied potential was observed ( $\approx 0.2 \text{ mA cm}^{-2}$  at 1.23 V<sub>RHE</sub>). Interestingly, sample 400\_H yielded a higher photocurrent density, that, despite being lower than that recorded in NaOH solutions (compare Figure 4a), reached *j* values of  $\approx 0.4 \text{ mA cm}^{-2}$  at 1.23 V<sub>RHE</sub>. This result, along with the previously discussed PEC data, shows that the obtained Fe<sub>2</sub>O<sub>3</sub>-TiO<sub>2</sub> materials represent a key step forward for the fabrication of photoanodes to be used in real-world devices.

### 2.3 TAS analysis on Fe<sub>2</sub>O<sub>3</sub>-TiO<sub>2</sub> photoanodes

To further elucidate the role of Fe<sub>2</sub>O<sub>3</sub>/TiO<sub>2</sub> heterojunctions in promoting the PEC water splitting and investigate charge carrier dynamics in the target photoelectrodes, transient absorption spectroscopy (TAS) analyses were carried out. TAS measurements allow the monitoring of photogenerated electron and hole dynamics from a picosecond to a second timescale,<sup>[57-59]</sup> and are a

powerful tool for the study of the interplay between nanostructure and PEC response in Fe<sub>2</sub>O<sub>3</sub> and TiO<sub>2</sub>-based photoanodes.<sup>[25,42,57,60,61]</sup> In this work, the evolution of charge carriers was examined by using band-gap excitation of both Fe<sub>2</sub>O<sub>3</sub> and TiO<sub>2</sub> at  $\lambda = 355$  nm, simulating the solar illumination conditions, in which light is absorbed by both components.

To investigate the electron mobility of TiO<sub>2</sub>-functionalized specimens, microsecond-to-millisecond TAS decays were measured at  $\lambda = 580$  nm. The selected probe wavelength corresponds to electrons trapped in *hematite* intra-band states and long-lived holes in both *hematite* and *anatase*.<sup>[57,58,62]</sup> Transient absorption traces and corresponding exponential fits for the specimens are displayed in Figure 5a. The initial photobleaching, *i.e.* the negative absorption change, following the excitation laser pulse could be assigned to the intra-band trapped electrons in *hematite*.<sup>[57]</sup> The fits resulted in lifetimes of 1.7 and 900 ms for bare Fe<sub>2</sub>O<sub>3</sub>, 0.5 and 550 ms for sample 400\_L, and 0.3 and 330 ms for sample 400\_H, respectively. The short-lived components correspond to the bleaching recovery, attributed to the extraction of trapped electrons, and are therefore indicative of electron mobility in the metal oxide structure. The increased bleaching recovery rate ( $1/\tau$ ) of 400\_L and 400\_H with respect to bare Fe<sub>2</sub>O<sub>3</sub> suggested enhanced electron mobility for the Fe<sub>2</sub>O<sub>3</sub>-TiO<sub>2</sub> heterostructure. TAS amplitude for 400\_L and 400\_H is higher with respect to bare Fe<sub>2</sub>O<sub>3</sub> (Figure 5a), indicating therefore higher amount of holes surviving the initial electron-hole recombination in the TiO<sub>2</sub> functionalized photoanodes. The long-lived components with the positive absorption were assigned to holes participating to water oxidation, and were resolved more accurately in a millisecond-to-second timescale (see below), in which water splitting has been reported to occur.<sup>[57,63]</sup>

The TAS decays of the specimens in a second time range at a probe wavelength of  $\lambda = 650$  nm, corresponding to the hole absorption in both Fe<sub>2</sub>O<sub>3</sub> and TiO<sub>2</sub>,<sup>[58,62]</sup> were fitted with an exponential model, shown in Figure 5b (see also SI, Figure S8). Functionalization of Fe<sub>2</sub>O<sub>3</sub> with TiO<sub>2</sub> decreased the lifetime of long-lived photoholes, as indicated by the mean lifetimes of 3.0 and 1.8 s obtained for the bare Fe<sub>2</sub>O<sub>3</sub> and 400\_L photoanodes, respectively. This phenomenon is in good agreement

with the higher PEC response of the TiO<sub>2</sub>-containing specimens, as it demonstrates the enhanced hole reaction rate with water. Previously published hole lifetimes for water oxidation over TiO<sub>2</sub> photoelectrodes were close to 0.3 s.<sup>[61,63]</sup> Hence, despite the presence of the TiO<sub>2</sub> overlayer, hole dynamics of specimen 400\_L are directly influenced by the presence of the underlying *hematite*. Moreover, a photohole lifetime of 0.5 s was obtained for specimen 400\_H (Figure 5b), **a lower value with respect to bare Fe<sub>2</sub>O<sub>3</sub> and 400\_L, as can be noticed already on a millisecond timescale (Figure 5). The uniform and thicker coverage of Fe<sub>2</sub>O<sub>3</sub> by TiO<sub>2</sub> in specimen 400\_H can be likely considered responsible for the higher PEC response of this photoanode in comparison to the 400\_L one.**

Picosecond TAS decays for the bare Fe<sub>2</sub>O<sub>3</sub>, 400\_L, and 400\_H photoanodes were compared at 580 nm to investigate the effect of TiO<sub>2</sub> functionalization on initial electron-hole recombination in Fe<sub>2</sub>O<sub>3</sub>. The retarded electron-hole recombination on the < 10 ps time range for the Fe<sub>2</sub>O<sub>3</sub>-TiO<sub>2</sub> specimens (SI, Figure S9) was assigned to the passivation of Fe<sub>2</sub>O<sub>3</sub> surface defects by TiO<sub>2</sub> deposition,<sup>[6]</sup> **favoring, in turn, a decrease** in detrimental charge recombination events.

To rationalize the obtained data, it is necessary to consider that the lower valence band energy of TiO<sub>2</sub> with respect to Fe<sub>2</sub>O<sub>3</sub> potentially prohibits hole transfer from Fe<sub>2</sub>O<sub>3</sub> to TiO<sub>2</sub>,<sup>[64]</sup> and this phenomenon should lead to a decreased PEC response. However, as demonstrated by Figure 4 and the related discussion, the photocurrent response of TiO<sub>2</sub>-functionalized specimens (**400\_L and 400\_H**) significantly outperforms that of the bare *hematite* (**Fe<sub>2</sub>O<sub>3</sub>**). Such a remarkable PEC enhancement **suggests** an efficient charge carrier separation upon coupling the two components in the resulting Fe<sub>2</sub>O<sub>3</sub>-TiO<sub>2</sub> **photoelectrodes**. In particular, **the role of the junction can be illustrated by analyzing the energy band diagram presented in Scheme 1, without (a) and with (b) an applied external bias.**<sup>[24,57,58,65]</sup> **The system Fermi level energy decreases with increasing positive bias, which further promotes band bending at the interfaces, an effect that becomes more pronounced upon raising the applied potential.** We propose that high photocurrents are achieved only after the valence band energy of *hematite* shifts to lower values with respect to the

TiO<sub>2</sub> valence band edge at the electrolyte interface, **promoting thus hole transfer from Fe<sub>2</sub>O<sub>3</sub> to TiO<sub>2</sub>. This conclusion is supported by the fact that no photocurrent plateau was observed for the TiO<sub>2</sub>-functionalized specimens (Figure 4), an effect attributed to an enhanced hole transfer through TiO<sub>2</sub> upon increasing the anodic potential, resulting, in turn, in a more pronounced band bending. In addition, hole conduction from Fe<sub>2</sub>O<sub>3</sub> to *titania via* TiO<sub>2</sub> electronic defect states can be considered as a possible alternative hole transport mechanism.<sup>[24]</sup>**

**On the basis of all the results, and taking into account that TiO<sub>2</sub> as such is not photoactive (see also SI, Figure S6), the high PEC response for the TiO<sub>2</sub>-functionalized specimens can be mainly explained basing on the formation of the Fe<sub>2</sub>O<sub>3</sub>-TiO<sub>2</sub> heterojunctions, promoting and improved separation of phogenerated charge carriers. In addition, band bending, becoming more important upon raising the applied external bias, further enhances spatial charge separation by hole tunneling through the TiO<sub>2</sub> overlayer (Scheme 1b).**

### 3. Conclusions

In conclusion, we have successfully prepared Fe<sub>2</sub>O<sub>3</sub>-TiO<sub>2</sub> nano-heterostructure photoanodes on FTO by the initial PE-CVD growth of Fe<sub>2</sub>O<sub>3</sub> nanosystems followed by ALD of TiO<sub>2</sub> layers with variable thickness and final annealing in air. The inherent benefits of the adopted joint process have enabled the fabrication of high-purity systems, characterized by an intimate contact between Fe<sub>2</sub>O<sub>3</sub> and TiO<sub>2</sub>. These features synergistically contributed to the extremely high performances in photoelectrochemical water oxidation activated by solar illumination, that corresponded to  $\approx 2.0$  mA cm<sup>-2</sup> photocurrent density at 1.23 V *vs.* RHE under simulated 1-sun irradiation. **The significant amplification in the PEC performance with respect to the case of bare Fe<sub>2</sub>O<sub>3</sub> was mainly attributed to the beneficial role of Fe<sub>2</sub>O<sub>3</sub>-TiO<sub>2</sub> heterojunctions, resulting in an enhanced charge separation and retarded electron-hole recombination.** In addition, TiO<sub>2</sub> protective action against corrosion has enabled the obtainment of attractive preliminary results even for PEC tests in seawater, whose use in solar water splitting is reported for the first time for Fe<sub>2</sub>O<sub>3</sub>-TiO<sub>2</sub> systems. These results, along with the high and stable photoanode activity, pave the way to sustainable energy generation starting from abundant and renewable natural resources through cost-effective nano-heterostructure devices. The proposed strategy and, in particular, the surface functionalization using ALD-deposited layers, may open doors to the use of combined synthesis approaches in the fabrication of a variety of nanostructures for photo-assisted applications displaying improved functionalities.

Basing on the present data, optimization of the material performances will require a fine tailoring of Fe<sub>2</sub>O<sub>3</sub> morphology, to obtain nanosystems endowed with higher porosity, and the investigation of higher TiO<sub>2</sub> loadings on such materials and on the ultimate functional behavior. Furthermore, detailed studies on the properties of the developed systems by incident photon-to-current efficiency (IPCE), external quantum efficiency (EQE) and impedance spectroscopy analyses will also be performed, in order to attain a detailed insight on the heterojunction properties.

## 4. Experimental Section

### 4.1 Synthesis

Fe<sub>2</sub>O<sub>3</sub> nanodeposits were fabricated using a custom-built two-electrode PE-CVD apparatus [radio frequency (RF) = 13.56 MHz; electrode diameter = 9 cm; inter-electrode distance = 6 cm].<sup>[41]</sup> Depositions were performed on previously cleaned<sup>[41,66]</sup> FTO-coated glass substrates (Aldrich, 735167-1EA,  $\approx 7 \Omega/\text{sq}$ ; lateral dimensions = 2.0 cm  $\times$  1.0 cm; FTO thickness  $\approx$  600 nm). Iron(III) oxide systems were prepared starting from Fe(hfa)<sub>2</sub>TMEDA (hfa = 1,1,1,5,5,5 - hexafluoro - 2,4 - pentanedionate; TMEDA = *N,N,N',N'* - tetramethylethylenediamine).<sup>[67]</sup> In a typical growth experiment, 0.30  $\pm$  0.01 g of precursor powders were placed in an external glass reservoir, heated by an oil bath at 65°C, and transported into the reaction chamber by electronic grade Ar [flow rate = 60 standard cubic centimeters per minute (sccm)]. In order to prevent undesired precursor condensation phenomena, connecting gas lines were maintained at 140°C by means of external heating tapes. Two additional gas inlets were used for the independent introduction of electronic grade Ar and O<sub>2</sub> (flow rates = 15 and 20 sccm, respectively) directly into the reaction chamber. After preliminary optimization experiments, each deposition was carried out for 1 h under the following conditions: growth temperature = 400°C; total reactor pressure = 1.0 mbar; RF-power of 10 W.

The as-prepared Fe<sub>2</sub>O<sub>3</sub> nanodeposits were subsequently coated with TiO<sub>2</sub> layers of different thickness by means of ALD. ALD experiments were performed at a deposition temperature of 150°C by a Ultratech/Cambridge Nanotech Inc Savanna 100 machine operating between 13-15 mbar, in continuous flow mode at 20 sccm. Titanium oxide was deposited starting from titanium(IV) tetra-isopropoxide [Ti(O<sup>*i*</sup>Pr)<sub>4</sub>] and milliQ water (H<sub>2</sub>O) as Ti and O sources, respectively. Ti(O<sup>*i*</sup>Pr)<sub>4</sub> was purchased from STREM Chemicals, Inc. (France) and used without any further purification. MilliQ water was produced by means of a Millipore DirectQ-5 purification system starting from tap water. The precursors were injected in the reactor directly from stainless steel reservoirs maintained at 80°C [Ti(O<sup>*i*</sup>Pr)<sub>4</sub>] and 25°C (H<sub>2</sub>O). Electronic grade N<sub>2</sub> was used as

carrier to feed the precursors vapours alternatively into the reaction chamber. To avoid precursor condensation, both valves and delivery lines were maintained at 115°C. After an initial pre-screening of the operating conditions, the use of thicker *titania* overlayers has been intentionally discarded in order to prevent the obtainment of too compact systems with reduced active area, a feature that could detrimentally affect the ultimate functional performances. After this optimization process, the cycle numbers were selected (Table 1) in order to obtain TiO<sub>2</sub> overlayers with the desired thickness.

After deposition, thermal treatments were carried out in air for 1 h at atmospheric pressure using a Carbolite HST 12/200 tubular furnace (heating rate = 20°C min<sup>-1</sup>) at 650°C. The use of higher temperatures was discarded, to prevent detrimental thermal degradations of FTO substrates.<sup>[43]</sup>

## 4.2 Characterization

FE-SEM analyses were carried out using a Zeiss SUPRA 40 VP FE-SEM instrument equipped with an Oxford INCA x-sight X-ray detector for EDXS investigation, operating at primary beam acceleration voltages comprised between 10.0 and 20.0 kV.

AFM analyses were run using a NT-MDT SPM Solver P47H-PRO instrument operating in semicontact/tapping mode and in air. After plane fitting, RMS roughness values were obtained from 3×3 μm<sup>2</sup> images.

SIMS investigation was performed by means of a IMS 4f mass spectrometer (Cameca) using a Cs<sup>+</sup> primary beam (voltage = 14.5 keV; current = 25 nA, stability = 0.2%) and negative secondary ion detection, adopting an electron gun for charge compensation. Beam blanking mode and high mass resolution configuration were adopted. Signals were recorded rastering over a 150×150 μm<sup>2</sup> area and detecting secondary ions from a sub-region close to 10×10 μm<sup>2</sup> in order to avoid crater effects.

XRD measurements were conducted operating in reflection mode by means of a Dymax-RAPID microdiffractometer equipped with a cylindrical imaging plate detector, allowing data collection from 0 to 160° (2θ) horizontally and from -45 to +45° (2θ) vertically upon using CuKα radiation (λ =

1.54056 Å). Each pattern was collected with an exposure time of 40 min, using a collimator diameter of 300 µm. Conventional XRD patterns were obtained by integration of 2D images.

TEM, HAADF-STEM and EDXS mapping experiments were carried out on a FEI Tecnai Osiris microscope, operated at 200 kV and equipped with a Super-X high solid angle energy-dispersive X-ray detector, as well as a FEI Titan “cubed” microscope (acceleration voltage = 200 kV), equipped with an aberration corrector for the probe-forming lens and a Super-X high solid angle EDXS detector.

XPS analyses were run on a Perkin-Elmer Φ 5600ci apparatus with a standard AlK $\alpha$  radiation ( $h\nu = 1486.6$  eV), at operating pressures  $< 10^{-8}$  mbar. Charge correction was performed by assigning to the adventitious C1s signal a Binding Energy (BE) of 284.8 eV.<sup>[68]</sup> After a Shirley-type background subtraction, atomic percentages (at. %) were calculated by signal integration using standard PHI V5.4A sensitivity factors.

Optical absorption spectra were recorded in transmission mode at normal incidence by means of a Cary 50 spectrophotometer, using bare FTO glass as a reference. In all cases, the substrate contribution was subtracted. Tauc plots were performed basing on Tauc equation, assuming the occurrence of direct allowed transitions.<sup>[41,43]</sup>

PEC measurements were performed in un-buffered 1 M NaOH solutions and, for selected systems, in simulated sea water (35 g/L sea salt from Tropic Marin), using a saturated calomel electrode (SCE) as reference, a Pt wire as counter-electrode and the Fe<sub>2</sub>O<sub>3</sub>-TiO<sub>2</sub> nanodeposits as working electrodes. A copper wire was soldered on an uncovered portion of the FTO substrate to establish electrical connection, and an epoxy resin was used to seal all exposed FTO portions, except for the electrode working areas.<sup>[69]</sup> Prior to measurements, the electrolyte was purged with N<sub>2</sub> to prevent any possible reaction with dissolved O<sub>2</sub>. Linear sweep voltammetry (10 mV/s) was carried out between -1.0 and 1.0 V vs. SCE using a potentiostat (PAR, Versa state IV), both in the dark and under front side illumination, using a Xe lamp (150 W, Oriel) with an AM 1.5 filter. Potentials with

respect to the reversible hydrogen electrode (RHE) scale ( $E_{\text{RHE}}$ ) were calculated using the Nernst equation:<sup>[35]</sup>

$$E_{\text{RHE}} = E_{\text{SCE}} + E_{\text{SCE}}^0 + 0.059 \text{ pH} \quad (1)$$

where  $E_{\text{SCE}}$  and  $E_{\text{SCE}}^0$  are the actual and standard potentials against SCE.

STH efficiency values are calculated basing of the following equation:<sup>[5,34]</sup>

$$\text{STH efficiency (\%)} = j \times (1.23 - E_{\text{RHE}}) / I_{\text{light}} \quad (2)$$

where  $E_{\text{RHE}}$  is the applied bias *vs.* RHE and  $I_{\text{light}}$  denotes the irradiance intensity (equal to 100 mW  $\text{cm}^{-2}$  for AM 1.5G illumination).

TAS experiments were performed on photoanodes having a geometric area of  $3 \times 3 \text{ cm}^2$  in a three-electrode PEC cell (Zahner-elektrik PECC-2) with a Pt counter-electrode, an Ag/AgCl (3 M KCl) reference electrode, and 0.1 M NaOH electrolyte (degassed with  $\text{N}_2$  prior to measurements). A potential value of 1.6 V *vs.* RHE was controlled by a standard potentiostat (CompactStat, Ivium Technologies) to probe the charge dynamics under water splitting conditions. TAS measurements in a microsecond-to-second timescale were carried out by a modified flash-photolysis apparatus (Luzchem LFP-111) with a New Focus (model 2051) photodetector and a halogen lamp (9 W, Thorlabs SLS201/M) probe. The excitation was fixed at  $\lambda = 355 \text{ nm}$ , with an energy density of  $0.4 \text{ mJ cm}^{-2}$ . The transient absorption traces were averaged 50–80 times. The microsecond-to-second decays are smoothed by using the Savitzky-Golay method with 25 smoothing point.

The picosecond-to-nanosecond TAS experiments were performed by a pump-probe system consisting of Libra F-1K (Coherent Inc.) generator producing 100 fs pulses at  $\lambda = 800 \text{ nm}$  (1 mJ) with a repetition rate of 1 kHz.<sup>[70]</sup> An optical parametric amplifier (Topas-C, Light Conversion Ltd.) was used to provide pump pulses at  $\lambda = 355 \text{ nm}$ . The measuring component was ExciPro (CDP Inc.) equipped with two array photodetectors coupled with a spectrometer (CDP2022i) set for probe detection in the 500–700 nm interval, with averaging over 10000 excitation shots. The maximum time

range available for probing was  $\approx 6$  ns. TAS decays were fitted by using exponential functions in order to elucidate the charge transfer processes and corresponding timescales in the studied photoanode systems.

## **Supporting Information**

Supporting Information is available from the Wiley Online Library or from the authors.

## **Acknowledgements**

The authors kindly acknowledge the financial support under the FP7 project “SOLAROGENIX” (NMP4-SL-2012-310333), as well as Padova University ex-60% 2012-2014 projects, grant n°CPDR132937/13 (SOLLEONE), and Regione Lombardia-INSTM ATLANTE projects. S.T. acknowledges the FWO Flanders for a post-doctoral scholarship.

## References

- [1] S. J. A. Moniz, S. A. Shevlin, D. J. Martin, Z.-X. Guo, J. Tang, *Energy Environ. Sci.* **2015**, *8*, 731.
- [2] R. Liu, Z. Zheng, J. Spurgeon, X. Yang, *Energy Environ. Sci.* **2014**, *7*, 2504.
- [3] W. H. Hung, T. M. Chien, A. Y. Lo, C. M. Tseng, D. D. Li, *RSC Adv.* **2014**, *4*, 45710.
- [4] P. Luan, M. Xie, X. Fu, Y. Qu, X. Sun, L. Jing, *Phys. Chem. Chem. Phys.* **2015**, *17*, 5043.
- [5] S. Hernández, V. Cauda, D. Hidalgo, V. Farías Rivera, D. Manfredi, A. Chiodoni, F. C. Pirri, *J. Alloys Compd.* **2014**, *615*, S530.
- [6] X. Yang, R. Liu, C. Du, P. Dai, Z. Zheng, D. Wang, *ACS Appl. Mater. Interfaces* **2014**, *6*, 12005.
- [7] M. Rioult, H. Magnan, D. Stanesco, A. Barbier, *J. Phys. Chem. C* **2014**, *118*, 3007.
- [8] D. Barreca, G. Carraro, V. Gombac, A. Gasparotto, C. Maccato, P. Fornasiero, E. Tondello, *Adv. Funct. Mater.* **2011**, *21*, 2611.
- [9] G. Carraro, C. Maccato, A. Gasparotto, T. Montini, S. Turner, O. I. Lebedev, V. Gombac, G. Adami, G. Van Tendeloo, D. Barreca, P. Fornasiero, *Adv. Funct. Mater.* **2014**, *24*, 372.
- [10] D. P. Cao, W. J. Luo, J. Y. Feng, X. Zhao, Z. S. Li, Z. G. Zou, *Energy Environ. Sci.* **2014**, *7*, 752.
- [11] G. K. Mor, H. E. Prakasam, O. K. Varghese, K. Shankar, C. A. Grimes, *Nano Lett.* **2007**, *7*, 2356.
- [12] L. Wang, C. Y. Lee, P. Schmuki, *Electrochem. Commun.* **2013**, *30*, 21.
- [13] X. J. Lian, X. Yang, S. J. Liu, Y. Xu, C. P. Jiang, J. W. Chen, R. L. Wang, *Appl. Surf. Sci.* **2012**, *258*, 2307.
- [14] C. X. Kronawitter, Z. Ma, D. Liu, S. S. Mao, B. R. Antoun, *Adv. Energy Mater.* **2012**, *2*, 52.
- [15] J. H. Kim, J. H. Kim, J.-W. Jang, J. Y. Kim, S. H. Choi, G. Magesh, J. Lee, J. S. Lee, *Adv. Energy Mater.* **2015**, *5*, 1401933.
- [16] P. Luan, M. Xie, D. Liu, X. Fu, L. Jing, *Sci. Rep.* **2014**, *4*, 6180.

- [17] O. Zandi, B. M. Klahr, T. W. Hamann, *Energy Environ. Sci.* **2013**, *6*, 634.
- [18] B. Klahr, S. Gimenez, F. Fabregat-Santiago, T. Hamann, J. Bisquert, *J. Am. Chem. Soc.* **2012**, *134*, 4294.
- [19] F. Le Formal, N. Tetreault, M. Cornuz, T. Moehl, M. Grätzel, K. Sivula, *Chem. Sci.* **2011**, *2*, 737.
- [20] L. Steier, I. Herranz-Cardona, S. Gimenez, F. Fabregat-Santiago, J. Bisquert, S. D. Tilley, M. Grätzel, *Adv. Funct. Mater.* **2014**, *24*, 7681.
- [21] H. Magnan, D. Stanescu, M. Rioult, E. Fonda, A. Barbier, *Appl. Phys. Lett.* **2012**, *101*, 133908.
- [22] S. Li, P. Zhang, X. Song, L. Gao, *Int. J. Hydrogen Energy* **2014**, *39*, 14596.
- [23] F. Le Formal, M. Grätzel, K. Sivula, *Adv. Funct. Mater.* **2010**, *20*, 1099.
- [24] S. Hu, M. R. Shaner, J. A. Beardslee, M. Lichterman, B. S. Brunschwig, N. S. Lewis, *Science* **2014**, *344*, 1005.
- [25] D. A. Wheeler, G. Wang, Y. Ling, Y. Li, J. Z. Zhang, *Energy Environ. Sci.* **2012**, *5*, 6682.
- [26] G. M. Carroll, D. K. Zhong, D. R. Gamelin, *Energy Environ. Sci.* **2015**, *8*, 577.
- [27] W.-H. Hung, T.-M. Chien, C.-M. Tseng, *J. Phys. Chem. C* **2014**, *118*, 12676.
- [28] D. Wang, X.-T. Zhang, P.-P. Sun, S. Lu, L.-L. Wang, Y.-A. Wei, Y.-C. Liu, *Int. J. Hydrogen Energy* **2014**, *39*, 16212.
- [29] C. Zhang, Q. Wu, X. Ke, J. Wang, X. Jin, S. Xue, *Int. J. Hydrogen Energy* **2014**, *39*, 14604.
- [30] Q. Yu, X. Meng, T. Wang, P. Li, J. Ye, *Adv. Funct. Mater.* **2015**, *25*, 2686.
- [31] M. Marelli, A. Naldoni, A. Minguzzi, M. Allieta, T. Virgili, G. Scavia, S. Recchia, R. Psaro, V. Dal Santo, *ACS Appl. Mater. Interfaces* **2014**, *6*, 11997.
- [32] S. C. Warren, K. Voitchovsky, H. Dotan, C. M. Leroy, M. Cornuz, F. Stellacci, C. Hébert, A. Rothschild, M. Grätzel, *Nat. Mater.* **2013**, *12*, 842.
- [33] Y. Lin, S. Zhou, S. W. Sheehan, D. Wang, *J. Am. Chem. Soc.* **2011**, *133*, 2398.

- [34] P. Sharma, P. Kumar, D. Deva, R. Shrivastav, S. Dass, V. R. Satsangi, *Int. J. Hydrogen Energy* **2010**, *35*, 10883.
- [35] G. Wang, Y. Ling, D. A. Wheeler, K. E. N. George, K. Horsley, C. Heske, J. Z. Zhang, Y. Li, *Nano Lett.* **2011**, *11*, 3503.
- [36] N. T. Hahn, C. B. Mullins, *Chem. Mater.* **2010**, *22*, 6474.
- [37] N. Mirbagheri, D. Wang, C. Peng, J. Wang, Q. Huang, C. Fan, E. E. Ferapontova, *ACS Catal.* **2014**, *4*, 2006.
- [38] Z. Fu, T. Jiang, Z. Liu, D. Wang, L. Wang, T. Xie, *Electrochim. Acta* **2014**, *129*, 358.
- [39] L. Xi, S. Y. Chiam, W. F. Mak, P. D. Tran, J. Barber, S. C. J. Loo, L. H. Wong, *Chem. Sci.* **2013**, *4*, 164.
- [40] M. H. Lee, J. H. Park, H. S. Han, H. J. Song, I. S. Cho, J. H. Noh, K. S. Hong, *Int. J. Hydrogen Energy* **2014**, *39*, 17501.
- [41] D. Barreca, G. Carraro, A. Gasparotto, C. Maccato, C. Sada, A. P. Singh, S. Mathur, A. Mettenbörger, E. Bontempi, L. E. Depero, *Int. J. Hydrogen Energy* **2013**, *38*, 14189.
- [42] S. Shen, C. X. Kronawitter, D. A. Wheeler, P. Guo, S. A. Lindley, J. Jiang, J. Z. Zhang, L. Guo, S. S. Mao, *J. Mater. Chem. A* **2013**, *1*, 14498.
- [43] M. E. A. Warwick, K. Kaunisto, D. Barreca, G. Carraro, A. Gasparotto, C. Maccato, E. Bontempi, C. Sada, T.-P. Ruoko, S. Turner, G. Van Tendeloo, *ACS Appl. Mater. Interfaces* **2015**, *7*, 8667.
- [44] C. H. Miao, T. F. Shi, G. P. Xu, S. L. Ji, C. H. Ye, *ACS Appl. Mater. Interfaces* **2013**, *5*, 1310.
- [45] S. J. A. Moniz, S. A. Shevlin, X. An, Z.-X. Guo, J. Tang, *Chem. Eur. J.* **2014**, *20*, 15571.
- [46] M. T. Mayer, Y. Lin, G. Yuan, D. Wang, *Acc. Chem. Res.* **2013**, *46*, 1558.
- [47] C. X. Kronawitter, L. Vayssieres, S. Shen, L. Guo, D. A. Wheeler, J. Z. Zhang, B. R. Antoun, S. S. Mao, *Energy Environ. Sci.* **2011**, *4*, 3889.

- [48] J. Y. Kim, G. Magesh, D. H. Youn, J.-W. Jang, J. Kubota, K. Domen, J. S. Lee, *Sci. Rep.* **2013**, *3*, 2681.
- [49] D. Barreca, G. Carraro, A. Gasparotto, C. Maccato, F. Rossi, G. Salviati, M. Tallarida, C. Das, F. Fresno, D. Korte, U. L. Stangar, M. Franko, D. Schmeisser, *ACS Appl. Mater. Interfaces* **2013**, *5*, 7130.
- [50] Z. Li, W. Luo, M. Zhang, J. Feng, Z. Zou, *Energy Environ. Sci.* **2013**, *6*, 347.
- [51] Y. Ling, G. Wang, D. A. Wheeler, J. Z. Zhang, Y. Li, *Nano Lett.* **2011**, *11*, 2119.
- [52] J. Luo, X. Xia, Y. Luo, C. Guan, J. Liu, X. Qi, C. F. Ng, T. Yu, H. Zhang, H. J. Fan, *Adv. Energy Mater.* **2013**, *3*, 737.
- [53] Pattern N° 33-0664, JCPDS (2000).
- [54] Pattern N° 00-021-1272, JCPDS (2000).
- [55] S. M. Ji, H. Jun, J. S. Jang, H. C. Son, P. H. Borse, J. S. Lee, *J. Photochem. Photobiol., A* **2007**, *189*, 141.
- [56] H. Joo, S. Bae, C. Kim, S. Kim, J. Yoon, *Sol. Energy Mater. Sol. Cells* **2009**, *93*, 1555.
- [57] M. Barroso, S. R. Pendlebury, A. J. Cowan, J. R. Durrant, *Chem. Sci.* **2013**, *4*, 2724.
- [58] S. R. Pendlebury, X. Wang, F. Le Formal, M. Cornuz, A. Kafizas, S. D. Tilley, M. Grätzel, J. R. Durrant, *J. Am. Chem. Soc.* **2014**, *136*, 9854.
- [59] B. C. Fitzmorris, J. M. Patete, J. Smith, X. Mascorro, S. Adams, S. S. Wong, J. Z. Zhang, *ChemSusChem* **2013**, *6*, 1907.
- [60] A. J. Cowan, W. Leng, P. R. F. Barnes, D. R. Klug, J. R. Durrant, *Phys. Chem. Chem. Phys.* **2013**, *15*, 8772.
- [61] J. Tang, J. R. Durrant, D. R. Klug, *J. Am. Chem. Soc.* **2008**, *130*, 13885.
- [62] A. J. Cowan, C. J. Barnett, S. R. Pendlebury, M. Barroso, K. Sivula, M. Grätzel, J. R. Durrant, D. R. Klug, *J. Am. Chem. Soc.* **2011**, *133*, 10134.
- [63] J. Tang, A. J. Cowan, J. R. Durrant, D. R. Klug, *J. Phys. Chem. C* **2011**, *115*, 3143.
- [64] J. B. Baxter, C. Richter, C. A. Schmuttenmaer, *Annu. Rev. Phys. Chem.* **2014**, *65*, 423.

- [65] L. Peng, T. Xie, Y. Lu, H. Fan, D. Wang, *Phys. Chem. Chem. Phys.* **2010**, *12*, 8033.
- [66] G. Carraro, A. Gasparotto, C. Maccato, E. Bontempi, F. Bilo, D. Peeters, C. Sada, D. Barreca, *CrystEngComm* **2014**, *16*, 8710.
- [67] D. Barreca, G. Carraro, A. Devi, E. Fois, A. Gasparotto, R. Seraglia, C. Maccato, C. Sada, G. Tabacchi, E. Tondello, A. Venzo, M. Winter, *Dalton Trans.* **2012**, *41*, 149.
- [68] D. Briggs, M. P. Seah, *Practical Surface Analysis: Auger and X-ray Photoelectron Spectroscopy*, John Wiley & Sons: New York, 2<sup>nd</sup> ed., 1990.
- [69] S. Kumari, A. P. Singh, Sonal, D. Deva, R. Shrivastav, S. Dass, V. R. Satsangi, *Int. J. Hydrogen Energy* **2010**, *35*, 3985.
- [70] D. Sirbu, C. Turta, A. C. Benniston, F. Abou-Chahine, H. Lemmetyinen, N. V. Tkachenko, C. Wood, E. Gibson, *RSC Adv.* **2014**, *4*, 22733.

<b>Sample ID</b>	<b>Fe<sub>2</sub>O<sub>3</sub> by PE-CVD</b>	<b>TiO<sub>2</sub> by ALD</b>	<b>Thermal Annealing</b>
<b>Fe<sub>2</sub>O<sub>3</sub></b>		//	
<b>400_L</b>	400°C, 1 h	150°C, 1150 cycles	650°C, 1 h, air
<b>400_H</b>		150°C, 5750 cycles	

**Table 1.** Main growth and processing conditions for FTO-supported photoanodes investigated in the present study.

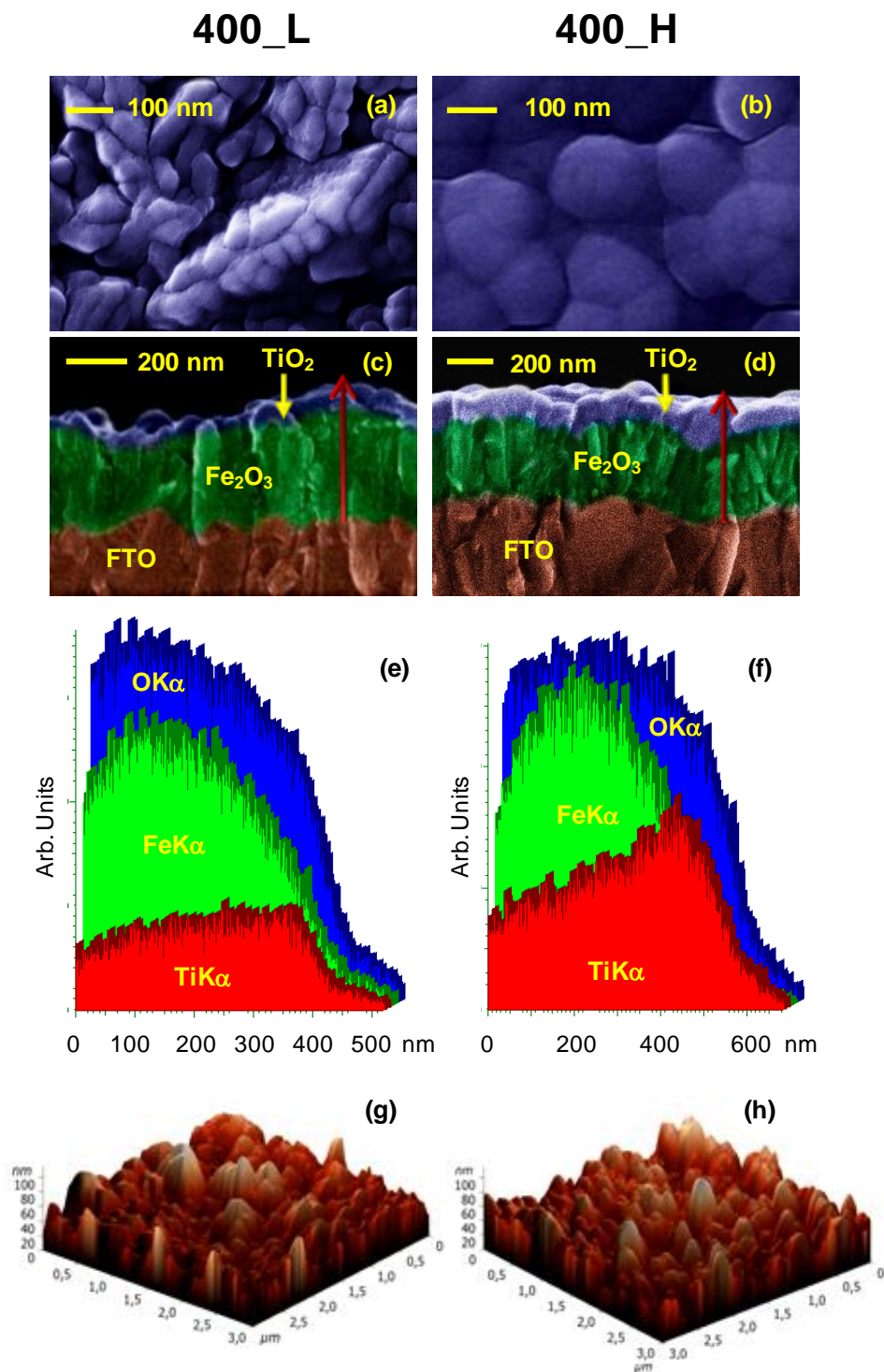


**Figure 1.** (a,b) Plane-view FE-SEM images, (c,d) cross-sectional FE-SEM images, (e,f) EDXS line-scan profiles recorded along the lines marked in cross-sectional views, and (g,h) AFM micrographs for  $\text{Fe}_2\text{O}_3$ - $\text{TiO}_2$  specimens. In (e) and (f), arrows mark the direction of abscissa increase.

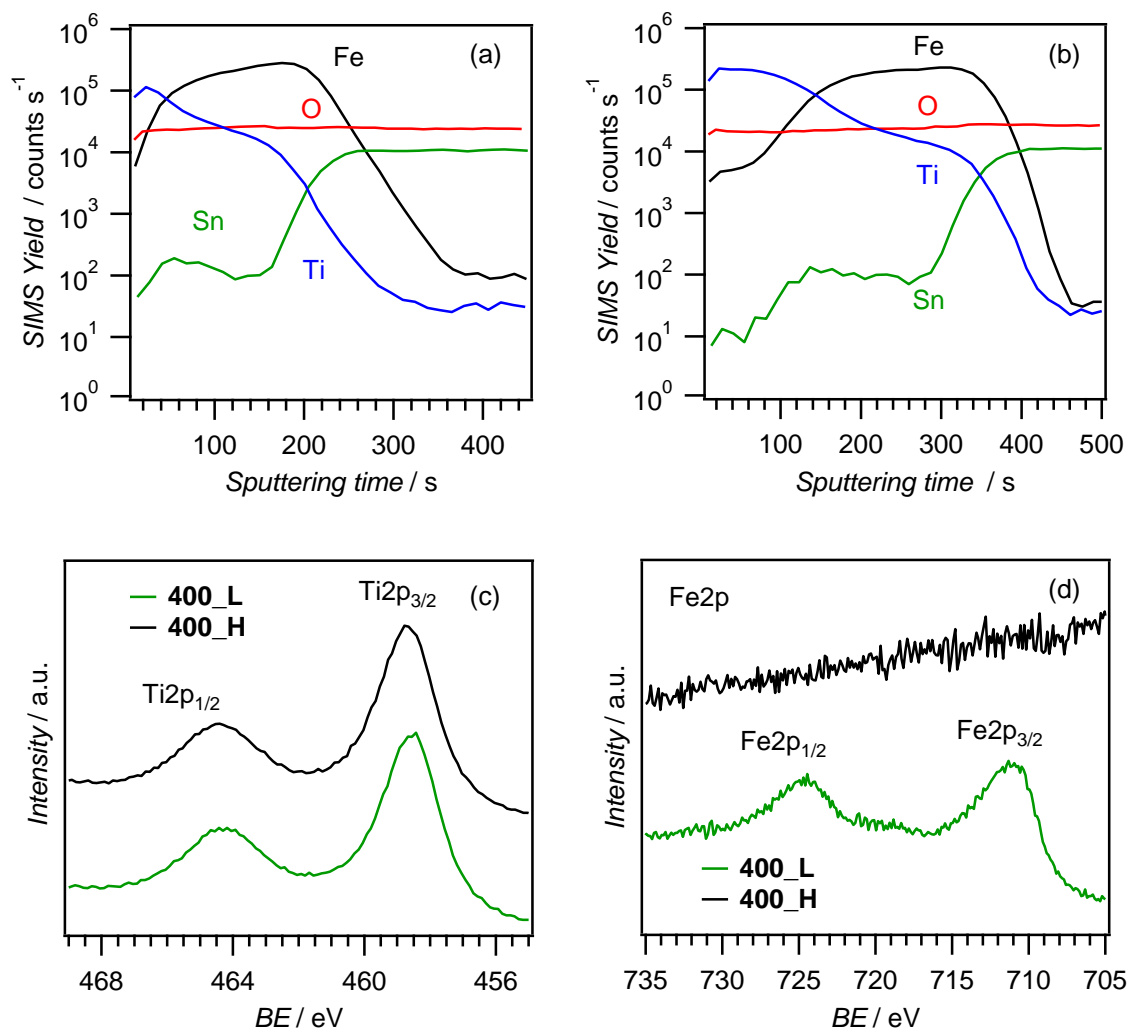


**Figure 2.** SIMS depth profiles for Fe<sub>2</sub>O<sub>3</sub>-TiO<sub>2</sub> deposits on FTO: (a) **400\_L**; (b) **400\_H**. (c) Ti2p, and (d) Fe2p XPS surface spectra for the same specimens.

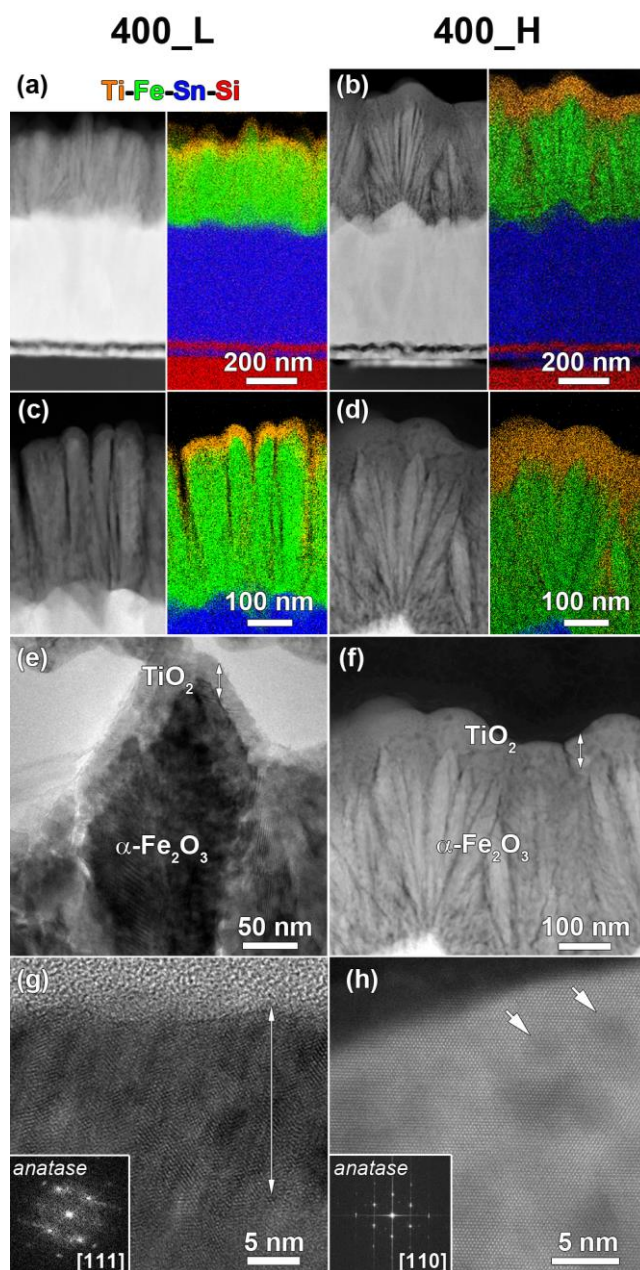


**Figure 3.** TEM characterization of Fe<sub>2</sub>O<sub>3</sub>-TiO<sub>2</sub> photoanodes. (a-d) Cross sectional HAADF-STEM images and corresponding EDXS chemical maps of samples **400\_L** (a,c) and **400\_H** (b,d). (e) TEM overview image of sample **400\_L**. (f) HAADF-STEM overview of sample **400\_H**. In both cases, the TiO<sub>2</sub> overlayer thickness is marked by a double-ended arrow. (g) HR-TEM image of sample **400\_L**, evidencing the low crystallinity of the *anatase* top layer. The *anatase* layer is imaged along the [111] zone axis, as evidenced by the inset Fourier transform (FT) pattern. (h) High resolution HAADF-STEM image of sample **400\_H**, with arrows indicating the presence of small dark-contrast voids in the highly crystalline *anatase* overlayer. The *anatase* layer is imaged along the [110] zone axis, as evidenced by the inset FT pattern.

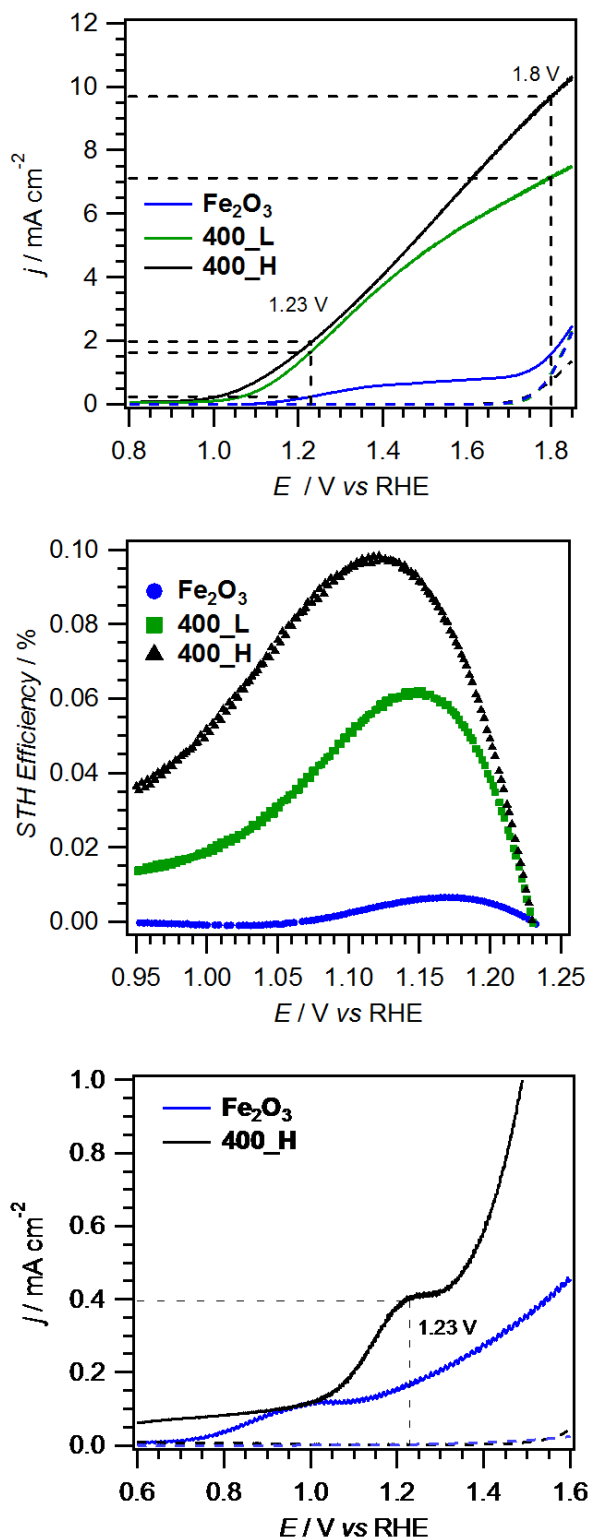


**Figure 4.** (a) Photocurrent density vs. applied potential curves for Fe<sub>2</sub>O<sub>3</sub> and Fe<sub>2</sub>O<sub>3</sub>-TiO<sub>2</sub> photoelectrodes recorded in 1 M NaOH solution under simulated solar irradiation (continuous lines) and in the dark (dashed lines). (b) Calculated solar-to-hydrogen (STH) efficiencies. (c)  $j$ - $E$  curves for bare Fe<sub>2</sub>O<sub>3</sub> and for specimen 400\_H in a simulated seawater solution, recorded under solar illumination. Dark current curves are reported as dashed lines.

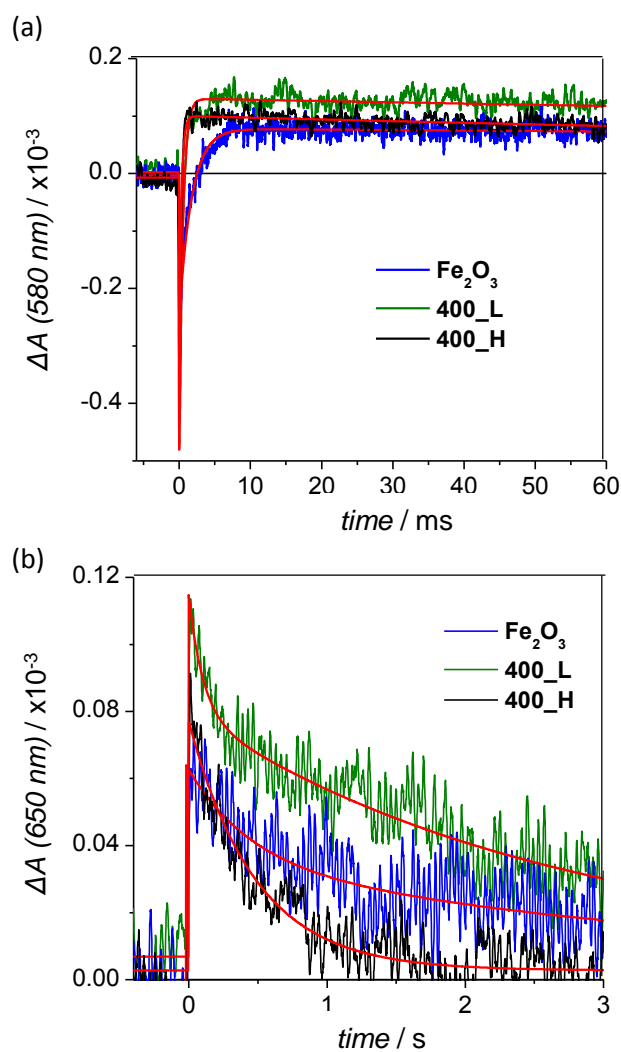
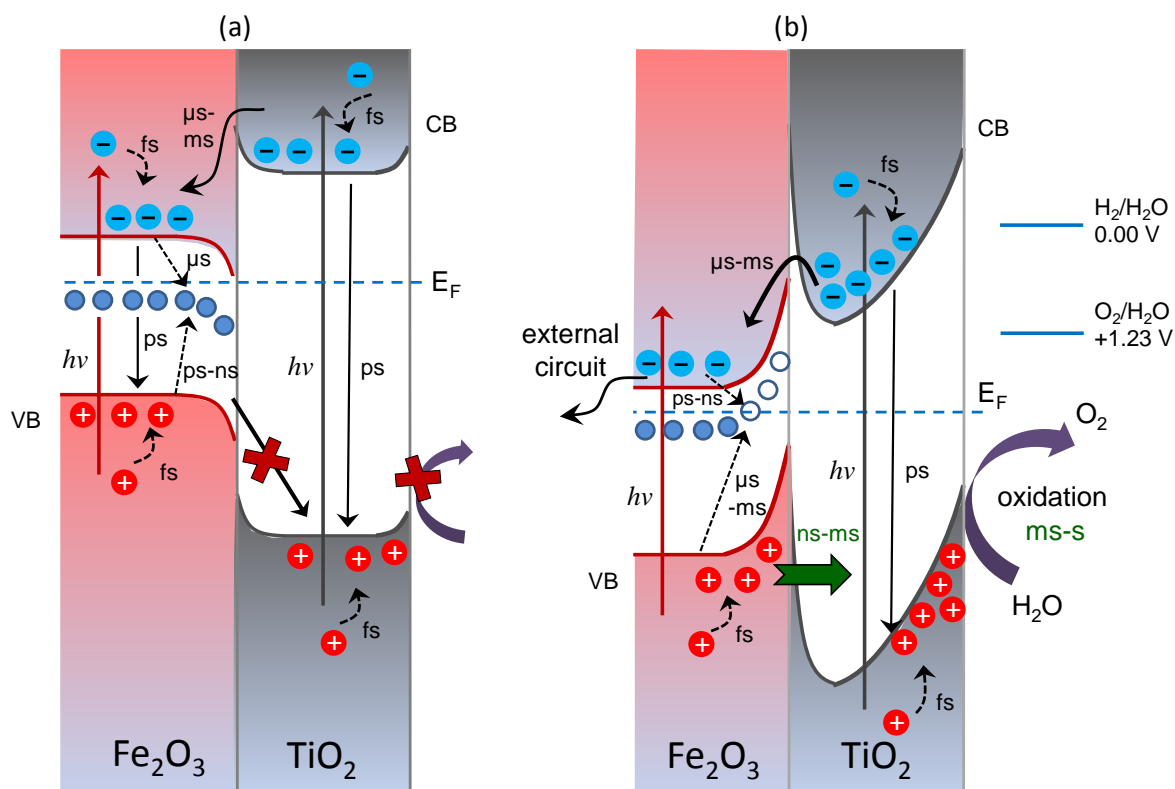


**Figure 5.** TAS decays for bare  $\text{Fe}_2\text{O}_3$  and  $\text{Fe}_2\text{O}_3\text{-TiO}_2$  samples on a millisecond (a) and a second (b) timescale. Red lines represent exponential fits of raw data.



**Scheme 1.** Schematic energy level diagrams illustrating the photo-activated charge transfer processes and related timescales: **(a) without, and (b) with the application of a positive external bias to  $\text{Fe}_2\text{O}_3$ - $\text{TiO}_2$  photoanodes.** The intra-band electron trap states, located a few 100 mV below the conduction band edge of *hematite*, are also shown. (CB: conduction band, VB: valence band,  $E_F$ : Fermi level, fs: femtosecond, ps: picosecond, ns: nanosecond,  $\mu$ s: microsecond, ms: millisecond)

## Table of contents entry

**Keywords:** Fe<sub>2</sub>O<sub>3</sub>; TiO<sub>2</sub>; nano-heterostructures; water splitting; photoelectrochemistry.

### Fe<sub>2</sub>O<sub>3</sub>-TiO<sub>2</sub> nano-heterostructure photoanodes for highly efficient solar water oxidation

Davide Barreca, Giorgio Carraro, Alberto Gasparotto, Chiara Maccato, Michael E.A. Warwick, Kimmo Kaunisto, Cinzia Sada, Stuart Turner, Yakup Gönüllü, Tero-Petri Ruoko, Laura Borgese, Elza Bontempi, Gustaaf Van Tendeloo, Helge Lemmetyinen, and Sanjay Mathur

**Fe<sub>2</sub>O<sub>3</sub>-TiO<sub>2</sub> photoanodes for photoelectrochemical water splitting** were fabricated on FTO substrates by a two-step vapor-phase synthetic strategy, followed by thermal annealing in air. The performances of  $\approx 2.0 \text{ mA cm}^{-2}$  photocurrent at 1.23 V vs. RHE under simulated solar irradiation, along with the system activity even in seawater, pave the way to the sustainable generation of renewable energy starting from abundant natural resources.

